PAPER

Multi-stoichiometric quasi-two-dimensional W_nO_{3n-1} tungsten oxides

Luka Pirker, [ID] *[a] Bojana Višić, [ID] [a,b] Srečo D. Škapin, [ID] [a,c] Goran Dražić, [ID] [a,c,d] Janez Kovač[a] and Maja Remškar [ID] [a]

Quasi-two-dimensional tungsten oxide structures, which nucleate by epitaxial growth on $W_{19}O_{55}$ nanowires (NW) and grow as thin platelets, were identified. Both the nanowires and the platelets accommodate oxygen deficiency by the formation of crystallographic shear planes. Stoichiometric phases, $W_{18}O_{53}$ ($WO_{2.944}$), $W_{17}O_{50}$ ($WO_{2.941}$), $W_{16}O_{47}$ ($WO_{2.938}$), $W_{15}O_{44}$ ($WO_{2.933}$), $W_{14}O_{41}$ ($WO_{2.929}$), $W_{10}O_{29}$ ($WO_{2.9}$), and W_9O_{26} ($WO_{2.889}$), syntactically grow inside a single platelet. These layered crystals show a new kind of polycrystallinity, where crystallographic shear planes accommodate oxygen deficiency and at the same time stabilize this multi-stoichiometric structure.

Introduction

Tungsten(VI) oxide (WO_3) is one of the best investigated transition metal oxides due to its various applications in photochromic smart windows,[1,2] optoelectronics,[3] gas sensing and photocatalysis,[4] as supercapacitors,[5] nanostructured thermoelectrics,[6] *etc*. WO_3 forms a rich variety of crystal structures composed of corner- and edge-sharing WO_6 octahedra, which differ in tilting angles, displacement of the W cation from the centre of the octahedron, and rotation of WO_6 octahedra with respect to an ideal cubic (ReO_3 type) structure.[7] In the bulk state, partially reversible interphase transformations occur upon heating, from monoclinic II (ε-WO_3) structure, stable below −43 °C, *via* triclinic (δ-WO_3) (−43 °C to 17 °C), monoclinic I (γ-WO_3) (17 °C to 330 °C), orthorhombic (β-WO_3) (330 °C to 740 °C), and tetragonal (α-WO_3) phase, stable above 740 °C.[8] In addition, a metastable hexagonal (h-WO_3) phase was reported, which on annealing transforms into a monoclinic structure at 400 °C.[9] At the nanoscale, the orthorhombic phase is already stable at room temperature and other phase transitions occur at lower temperatures than in the bulk state.[10] A decrease in phase transition temperature depends on the size of WO_3 nanoparticles.[11] Different particular particle shapes were obtained *via* various growth techniques, such as pseudo-

spherical nanometre-sized particles, NWs, nano-discs and flakes.[12]

Recently, two-dimensional (2D) nanostructures including 2D-WO_3, have attracted a lot of attention among researchers due to novel physical and chemical properties, which differ from their bulk counterparts: high surface area; appearance of crystalline planes/surfaces which are not available in bulk materials; stability of crystal phases declared as metastable *etc*. The first WO_3 crystals with a plate-like shape were prepared using a wet chemical route from $H_2WO_4 \cdot H_2O$ precursor crystals with poly(ethylene glycol) as the surface modulator, which inhibited crystal growth in the [010] direction.[13] Other methods were also developed to obtain low-dimensional WO_3 materials.[14–16]

Besides stoichiometric WO_3, many sub-stoichiometric WO_{3-x} phases exist. They are often referred to as Magnéli phases with the chemical formula W_nO_{3n-1} or W_nO_{3n-2}.[17] The W_nO_{3n-1} and W_nO_{3n-2} series of tungsten oxides were thoroughly studied in the past, but only few phases with a known stoichiometry were directly observed.[18–36] They grow in similar structures to those of tungsten bronzes with the general formula A_xWO_3, where A is an electropositive element. In the tungsten bronzes, the W^{5+} state appears due to the presence of an electropositive element, whereas in WO_{3-x} it occurs through the intrinsic oxygen vacancies. These oxygen vacancies increase electrical conductivity through the formation of shallow donor states[37] and enhance photocurrent density by filling electron states, which act as electron traps and extend the lifetime of photoelectrons.[38] Therefore, WO_{3-x} materials can be used as sensors[39] for optoelectrical devices,[40] photocatalysis,[41,42] electrochromic devices,[43] *etc*. The crystal structure of WO_{3-x} compensates the advanced oxygen deficiency by creating crystallographic shear (CS) planes, where some of the corner-sharing WO_6 octahedra become

[a]Jožef Stefan Institute, Jamova 39, 1000 Ljubljana, Slovenia.
E-mail: luka.pirker@ijs.si
[b]Institute of Physics Belgrade, University of Belgrade, Pregrevica 118, 11080 Belgrade, Serbia
[c]Jožef Stefan International Postgraduate School, Jamova cesta 39, 1000 Ljubljana, Slovenia
[d]National Institute of Chemistry, Hajdrihova 19, 1001 Ljubljana, Slovenia

edge-sharing octahedra.[17] Further reduction of the material forces the WO_6 octahedra to share even more oxygen atoms. At a certain point, pentagonal columns and hexagonal channels with an equatorial edge and face-sharing WO_6 octahedra emerge as in the case of $W_{18}O_{49}$ and W_5O_{14}.[44–47] As previously shown,[17,48,49] tungsten oxides crystallize in a monoclinic unit cell with the symmetry $P2/m$, $P2/a$, $P2/c$ or $C2/c$. According to Magnéli,[17] the M_nO_{3n-1} (M = Mo and W) structures crystalize with the metal atoms forming puckered or non-puckered layers. The XRD results published in the literature show that all known W_nO_{3n-1} structures crystallize with the metal atoms forming puckered layers and thus the unit cell is composed of two M_nO_{3n-1} units with the $P2/a$ symmetry. Oxygen vacancies can also stabilize high symmetry phases at room temperature (RT), even a cubic one.[50] This is not the case in stoichiometric bulk WO_3, where only low-symmetry structures are stable at RT. As an example, W_5O_{14},[45] which belongs to W_nO_{3n-1} Magnéli's series, grows along the [001] crystal axis in the shape of NWs with a diameter below 150 nm in the tetragonal symmetry. Less reduced $W_{19}O_{55}$ rods[51,52] and $W_{25}O_{73}$[27] needles, both belonging to W_nO_{3n-2} series, grow in the monoclinic symmetry in the [010] direction.

Here, we report new two-dimensional and quasi-two-dimensional tungsten suboxide structures which grow epitaxially on the $W_{19}O_{55}$ nanowires (NWs). High-resolution electron microscopy (HRTEM) and transmission electron diffraction (TED) were used for structure determination, together with X-ray diffraction (XRD), photoelectron spectroscopy (XPS) and Raman spectroscopy.

Results and discussion

Electron microscopy investigation of the morphology and lattice structure

The platelets were found to be growing only from the $W_{19}O_{55}$ NWs, while the $W_{19}O_{55}$ NWs can exist without the platelets. The platelets grow with their b axis parallel to the b axis of the NWs. In several cases, the platelets were found to be terminated by the NWs at both edges. Inbuilt strain, likely caused by the lattice mismatch between the platelets and NWs, is manifested as extinction contours, and is partially relaxed by cracks visible as lines originating from the plate–NW interface (Fig 1a). The platelets grow up to 4 μm in lateral size and are
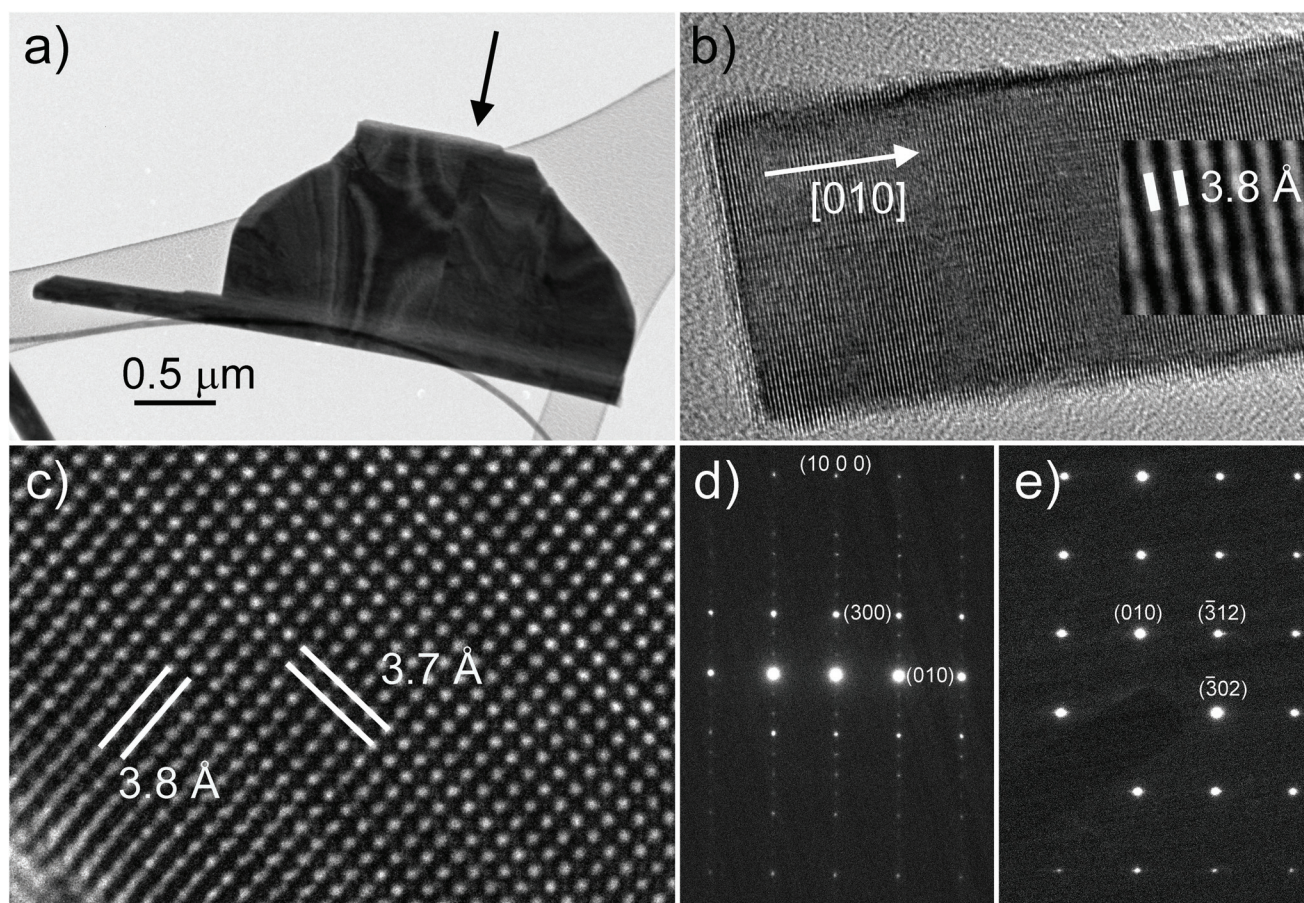

Fig. 1 TEM micrographs: (a) a plate with a defect line (marked with an arrow) and extinction contours revealing relaxation of the inbuilt strain; (b) a single $W_{19}O_{55}$ NW grown along the [010] direction with 3.8 Å periodicity along the NW length (inset); (c) the HRTEM image of the NW. (d) TED patterns of the [001] and (e) [203] zones of the $W_{19}O_{55}$ NW.

of rectangular shape. The thickness of the platelets is in a range of 100 ± 10 nm.

A single $W_{19}O_{55}$ NW is shown in Fig. 1b. The $W_{19}O_{55}$ NW grows along the [010] direction. The periodicity between atomic columns along the NW is 3.8 Å (Fig. 1b inset), which is in good agreement with the (010) interlayer distance (3.787 Å) of the monoclinic $W_{19}O_{55}$ (PDF 00-045-0167).[52] The HRTEM image of the NW shows a rectangular lattice with 3.8 Å and 3.7 Å (Fig. 1c), which agrees with the (010) and (302) planes of $W_{19}O_{55}$. The TED images show the [001] (Fig. 1d) and the [203] zones (Fig. 1e) of the monoclinic $W_{19}O_{55}$.

Fig. 2a–c show the group of randomly oriented platelets on a Si wafer and single platelets selected for making cross-sectional lamellas for TEM investigation. Two lamellas were prepared, one perpendicular to the NW (Fig. 2b, line B) and another parallel to the NW (Fig. 2c, line A). The TEM images of both lamellas are shown in Fig. 2d and e. Silicon was used as a substrate for the lamella B and molybdenum for the lamella A. The lamellas reveal that the platelets are thinner than the NWs (Fig. 2d) and that the free sides of the platelets are of rectangular shape (Fig. 2e). The lamella A reveals that the platelets are segmented with the interfaces oriented parallel to the free crystal edges (marked with black arrows, Fig. 2e). This segmentation can explain the outer shape of the platelets and a mechanical instability visible as a crack in Fig. 2c (white arrow).

Three viewing directions were investigated with the electron beam in a direction quasi-perpendicular to the cross-sections A and B (lamella A and lamella B), and quasi-perpendicular to the basic planes of the flakes. The term "quasi" is used because the samples were tilted and rotated under electron beam to obtain one of the central Laue zones.

The whole lamella B shown in Fig. 3a reveals a semi-periodic contrast, which is parallel to the basic planes of the platelets visible at upper left and lower right corners of the image. Fig. 3b shows the TEM image of the junction between the platelet and the $W_{19}O_{55}$ NW. The junction represents a transition area (marked with a white arrow) that compensates the lattice mismatch between the two structures. The transition area extends through the whole thickness of the platelet.

The HRTEM images (Fig. 3c, e, g and i) revealed that the contrast lines in Fig. 3a are crystallographic shear (CS) planes, which are typical of tungsten suboxides. The CS planes can be described in terms of $\{hkl\}_r$ planes of WO_3, which crystalize in the ReO_3-type structure.[20] In the case of the lamella B, only $\{102\}_r$ CS planes are observed. The atoms of the layers between the CS planes are regularly distributed in a nearly rectangular lattice with the parameters parallel and perpendicular to the CS planes being 3.83 Å and 3.91 Å, respectively. The angle between the atomic lines of the lattice between the CS planes is 89° ± 1°. Various distances between CS planes determine the stoichiometry of individual layers. Seven different structures are visible directly from the HRTEM images: $W_{18}O_{53}$ ($WO_{2.944}$), $W_{17}O_{50}$ ($WO_{2.941}$), $W_{16}O_{47}$ ($WO_{2.938}$), $W_{15}O_{44}$ ($WO_{2.933}$), $W_{14}O_{41}$ ($WO_{2.929}$), W_9O_{26} ($WO_{2.889}$) and $W_{10}O_{29}$ ($WO_{2.9}$). These structures are the members of the homologous series of tungsten

oxides with the formula W_nO_{3n-1}. Their existence was predicted,[17] but only $W_{10}O_{29}$ was experimentally observed to date.[17] Most of the layers crystallized in the $W_{16}O_{47}$ and $W_{15}O_{44}$ phases. Close to the thickness centre of the lamella, a defect in periodicity is visible. A layer of $W_{16}O_{47}$ is split into two layers forming the W_9O_{26} and $W_{10}O_{29}$ phases. For each phase, the unit cell parameters a and c were determined from the HRTEM images (Fig. 3), while the cell parameter b, which is the same in all phases, was determined from TEDs in Fig. 4. The results are summarized in Table 1.

The unit cell parameters of phases with different stoichiometries were also calculated using the model proposed in ref. 17, which was constructed for an ideal W_nO_{3n-1} structure grown in the $P2/a$ symmetry, where W atoms, which are not a part of CS planes, are equally separated. The input data for this model are the distance between tungsten atoms outside and inside CS planes and the number of tungsten atoms in a unit cell. The average interatomic distance (3.87 Å) between tungsten atoms that are not a part of the CS plane and between tungsten atoms in octahedra joined by edges (3.21 Å), which constitute the CS plane, was determined by HRTEM. As seen from Table 1, the calculated values are in relatively good agreement with the measured ones. The unit cells are schematically drawn on the HRTEM images and on the calculated structures in Fig 3. Strongly deformed hexagonal and pentagonal tunnels are concentrated at the CS planes (schematically shown in Fig. 3).

The platelets are thin enough for a direct TEM observation with basal planes exposed to the electron beam, so that transmission electron diffraction (TED) patterns in three perpendicular directions through the platelets could be obtained. Because the platelets are not single crystals but are composed of layers with different stoichiometries, the TEDs performed with the selected area diaphragm with a diameter of 140 nm represent an average structure of the investigated platelet.

Fig. 4 shows TEDs: (a) the [100] zone (lamella A), (b) the [010] zone (lamella B), and the [001] zone (basal plane). The main reflections in Fig. 4a can be indexed as the (010) and (0 0 10) reflections of the $W_{15}O_{44}$ phase. The reflections correspond to the interlayer distances of 3.72 Å and 2.60 Å, respectively. The (010) reflection is used for the first estimation of the unit cell parameter b, i.e. 3.72 Å. The second value (3.96 Å) of the parameter b was obtained from the (010) reflection in Fig. 4c, which represents the [001] zone. The mean value of the unit cell parameter b is 3.8 Å. This value was considered as the parameter b for all the phases in Table 1, as it should be the same for all W_nO_{3n-1} stoichiometries. Similarly, the parameter a should be the same for all phases. The first estimation of the parameter a was obtained from the (100) reflection in Fig. 4c corresponding to the interlayer distance of 17.18 Å. The intense reflection in this array is assigned to (10 0 0). Because of the $P2/a$ symmetry, only $(2n\ 0\ 0)$ reflections should be visible. The odd reflections could arise due to the thinness of the platelets and/or layers. The second value of the parameter a, which was determined from the reflection (10 0 0) from Fig. 4b, was 16.3 Å. The average value of the unit cell para-
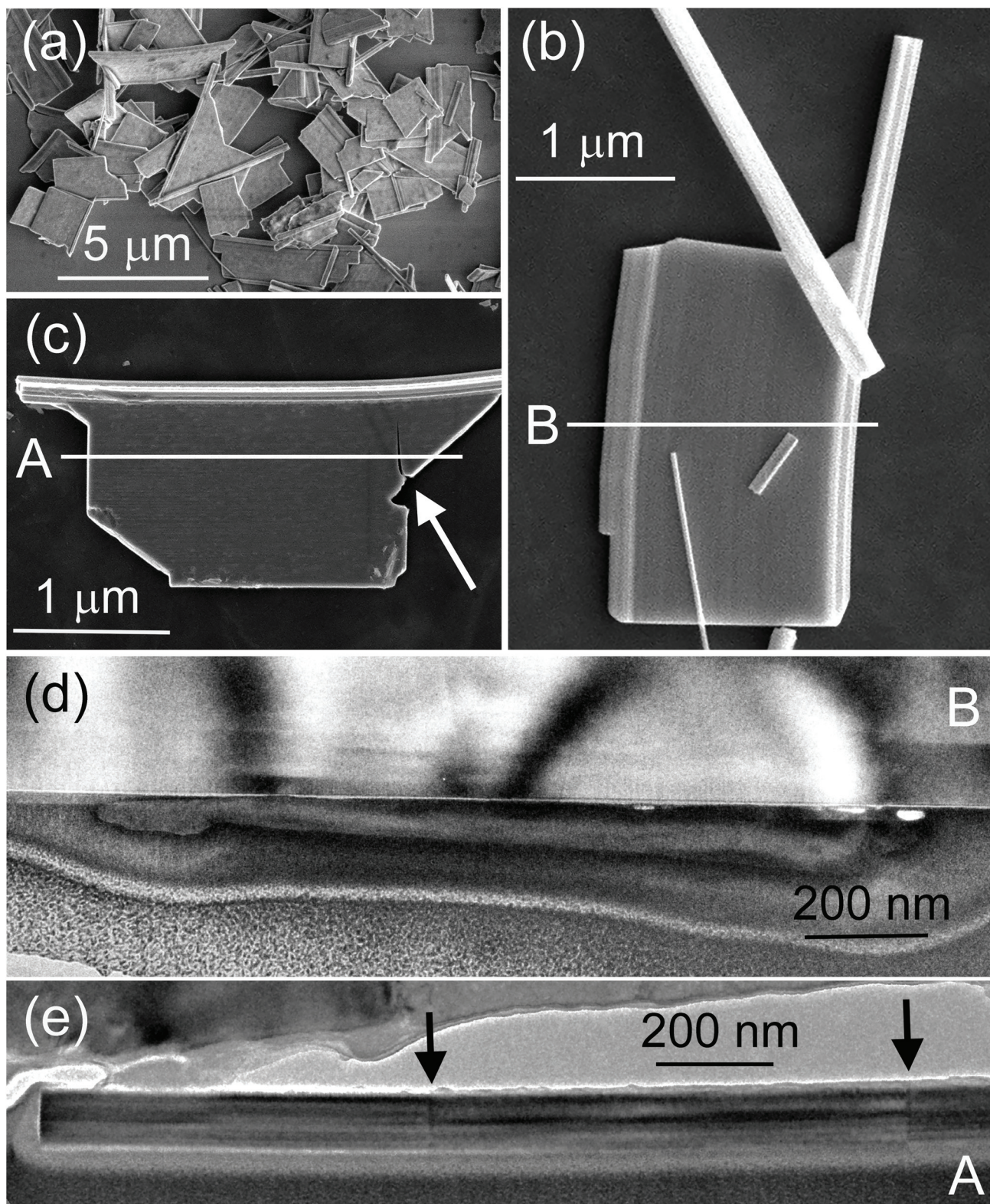
Fig. 2 SEM and TEM images of platelets: (a) randomly oriented platelets; (b and c): single platelets with the lines *a* and *b* labelling directions of the cross-sections for the TEM lamellas; (d) TEM image of the *b* cross-section with the Si wafer above and sputtered Pt below the platelet; (e) TEM image of the *a* cross-section.
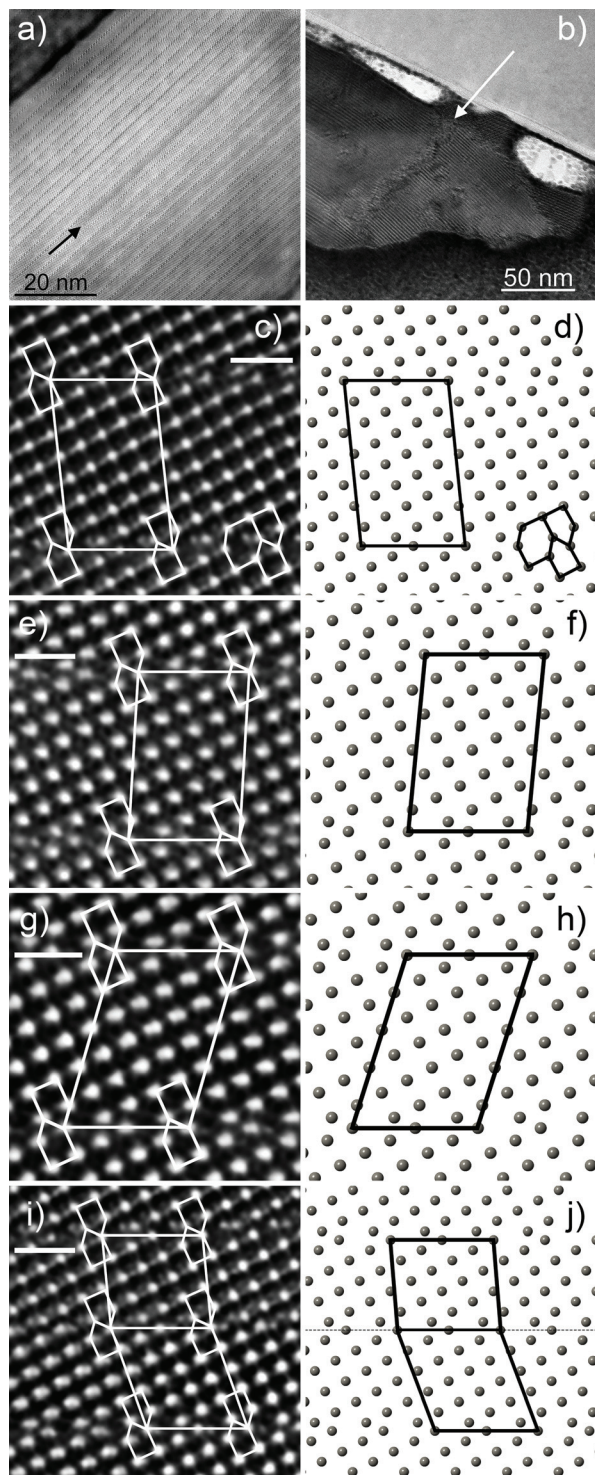
meter a is 16.7 Å. The diffraction in Fig. 4b was indexed using the unit cell parameter a = 16.3 Å, b = 3.8 Å, c = 22.6 Å and β = 94.1°. The parameter c (22.6 Å) was obtained from the reflection (0 0 14) corresponding to the interlayer distance of 1.61 Å. Only (2n 0 0) reflections are observed in Fig. 4b, which match with the extinction rules of the $P2/a$ symmetry.

As the parameter c is specific for each particular W_nO_{3n-1} phase, the obtained values represent only the parameter of a nominal unit cell of the average structure of the whole lamella. The parameter c was determined only with the purpose to explain the electron diffraction data.

Fig. 4d shows the schematic representation of the $W_{19}O_{55}$ NW and the platelet. The platelets grow with the a axis perpendicular to the NW. By calculating the b axis and c axis mismatch between the $W_{19}O_{55}$ NW and the platelet that predominantly grows in the $W_{16}O_{47}$ phase, one gets a mismatch of 1.7% and 19.8%, respectively (the unit cell parameters of the $W_{19}O_{55}$ phase: a = 12.13 Å; b = 3.793 Å; c = 22.45 Å; β = 94.5° (ref. 52)). While the mismatch in the b axis is small, the mismatch in the c axis is too large for the epitaxial growth of the platelets directly from the NW. This large mismatch might be the origin of stabilization of multi-stoichiometric crystals and is compensated in the transition area which separates the NW from the platelet. According to the literature,[53,54] the less reduced W_nO_{3n-1} phases with the $\{102\}_r$ CS planes nucleate first, and only after further reduction the W_nO_{3n-2} phases with the $\{103\}_r$ CS planes start to grow. In the presented case, the less reduced platelets seem to grow on the more reduced NWs. Considering that all stoichiometries inside platelets are less reduced than inside $W_{19}O_{55}$ nanowires, it is possible to assume that the platelets start to grow at the edges of the first nanowires, when the partial pressure of oxygen in ampoules is still sufficient. This is supported by our findings that the platelets form even when the transport reaction time is reduced to 72 hours. Because the directions of CS planes in the nanowires align with the CS planes of the platelets, the nanowires could act as templates for the platelets during growth. It is also possible that nickel acts as a growth promoter for the nanowires and further at the interface between nanowires and nanoplates,[55] but this assumption needs to be proved in future studies.

The synthesized material is composed of NWs and platelets with different stoichiometries. The distribution and the frequency of different stoichiometries between the different morphologies were not determined as it would be very time consuming due to the multi-stoichiometric structure of single crystals.

XRD analysis

A typical XRD spectrum of the platelets is shown in Fig. 5. With the help of the HRTEM images, where the $W_{16}O_{47}$ stoichiometry was identified as the dominant phase, this phase was used as a starting model for the average structure of the platelets. The unit cell parameters a, b, c, and β were refined using the assigned positions of the XRD peaks. In the refinement process, the presence of the $W_{19}O_{55}$ component of the

Fig. 3 HRTEM images of the lamella B: (a) the whole thickness with semi-regularly distributed CS planes, the arrow points to the defect; (b) transition area between the platelet and the NW; HRTEM image of: (c) $W_{16}O_{47}$ ($WO_{2.938}$), (e) $W_{15}O_{44}$ ($WO_{2.933}$), (g) $W_{14}O_{41}$ ($WO_{2.929}$), (i) W_9O_{26} ($WO_{2.889}$) and $W_{10}O_{29}$ ($WO_{2.9}$) with the proposed unit cell. The scale bar is 1 nm; (d) the simulated structures of: (d) $W_{16}O_{47}$ ($WO_{2.938}$); (f) $W_{15}O_{44}$ ($WO_{2.933}$), (h) $W_{14}O_{41}$ ($WO_{2.929}$), (j) W_9O_{26} ($WO_{2.889}$) and $W_{10}O_{29}$ ($WO_{2.9}$) with the proposed unit cells. The positions of the W atoms in the simulated structures were calculated according to ref. 17. In (j), the models of W_9O_{26} and $W_{10}O_{29}$ were joined, the dashed line shows the plane where the models were joined.
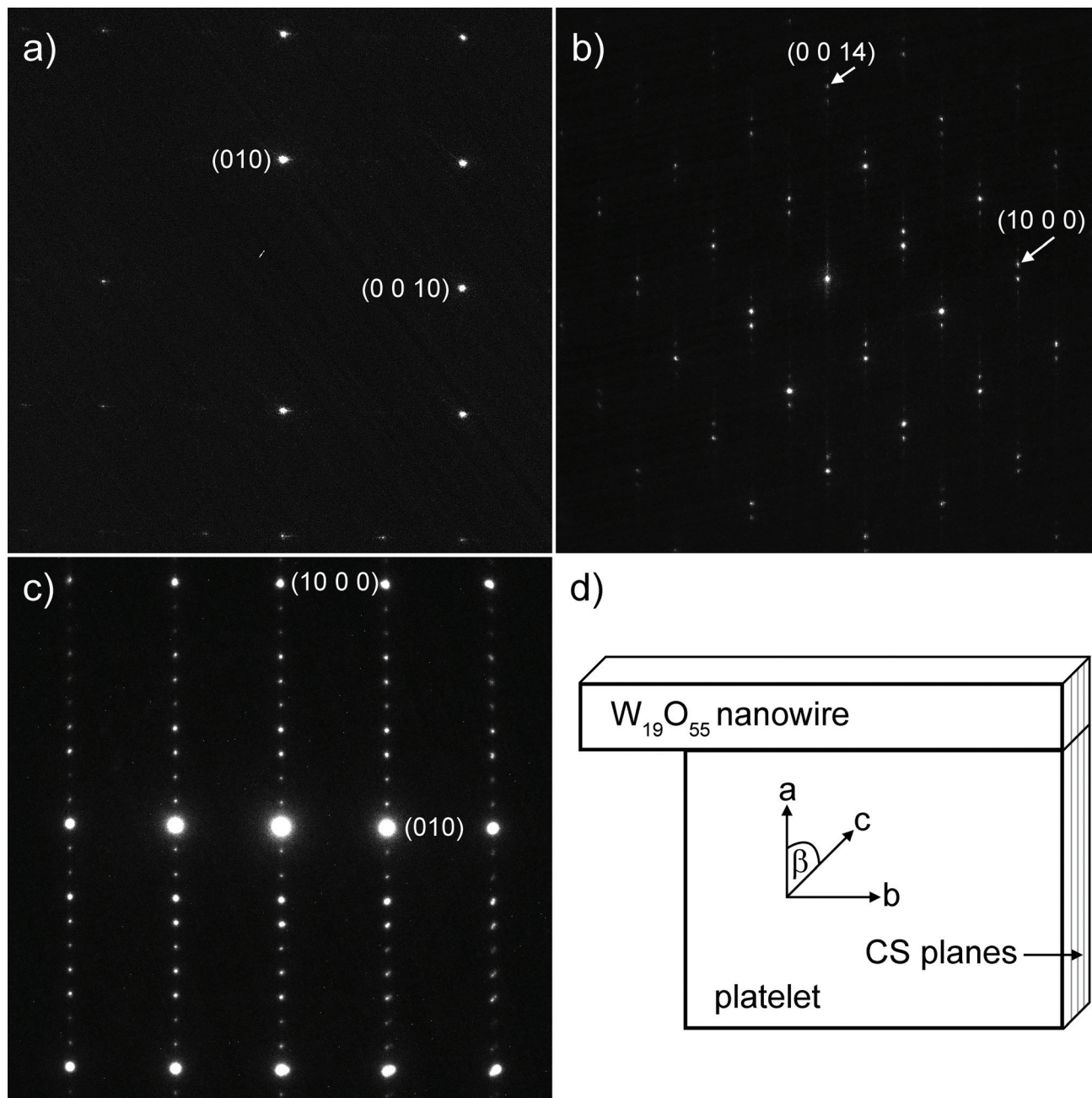
Fig. 4 TED patterns: (a) the [100] zone taken on the lamella A, (b) the [010] zone taken on the lamella B, and (c) the [001] zone taken perpendicular to the basal plane of the plate. (d) Schematically represented the relationship between the $W_{19}O_{55}$ NW and platelet axis.

Table 1 Measured and calculated unit cell parameters a, b, c and β

Structure	Measured				Calculated			
	a [Å]	b [Å]	c [Å]	β [°]	a [Å]	b [Å]	c [Å]	β [°]
W_9O_{26}	17.15	3.8	15.72	94.20	17.31	>3.87	15.31	94.29
$W_{10}O_{29}$	17.21	3.8	18.36	108.98	17.31	>3.87	18.14	110.44
$W_{14}O_{41}$	17.10	3.8	25.70	72.96	17.31	>3.87	25.08	72.58
$W_{15}O_{44}$	16.90	3.8	26.14	86.02	17.31	>3.87	25.76	84.84
$W_{16}O_{47}$	17.16	3.8	28.01	95.57	17.31	>3.87	27.54	96.00
$W_{17}O_{50}$	17.20	3.8	30.82	73.77	17.31	>3.87	30.55	72.40
$W_{18}O_{53}$	17.15	3.8	31.35	83.72	17.31	>3.87	31.11	82.53

Fig. 5 XRD spectrum of the platelets.

Table 3 Experimental, calculated and refined unit cell parameters of $W_{16}O_{47}$

$W_{16}O_{47}$ phase	a [Å]	b [Å]	c [Å]	β [°]
From HRTEM	17.16	3.80	28.01	95.57
Model	17.31	>3.87	27.54	96.00
Refined from XRD	16.04	3.88	28.48	96.07

matching of the unit cell parameters confirms that the majority of the layers in the platelets indeed grow in the $W_{16}O_{47}$ stoichiometry.

X-ray photoelectron spectroscopy (XPS) studies

The XPS measurement was performed on platelets, deposited on conductive carbon tape. The spectra were calibrated using the C 1s peak at 284.6 eV originating from adsorbed molecules and carbon tape. Traces of SiO_2, nickel and iodine were found sporadically in the sample. They are the remains from the reactants and the quartz ampule, where the sample was grown.

The tungsten peak comprising W 4f photoelectrons (Fig. 6a) shows the presence of several oxidation states. The peaks centred at 35.4 eV, 37.5 eV and 41.6 eV represent the emission from W $4f_{7/2}$, $4f_{5/2}$, and $5p_{3/2}$ core levels from the W atoms in the +6 oxidation state. The peaks centred at 33.9 eV, 36.7 eV, and 39.1 eV result from the emission from $4f_{7/2}$, $4f_{5/2}$, and $5p_{3/2}$ core levels from the W atoms in the +5 oxidation state.[56] No W atom peaks with the +4 oxidation state were observed.[57]
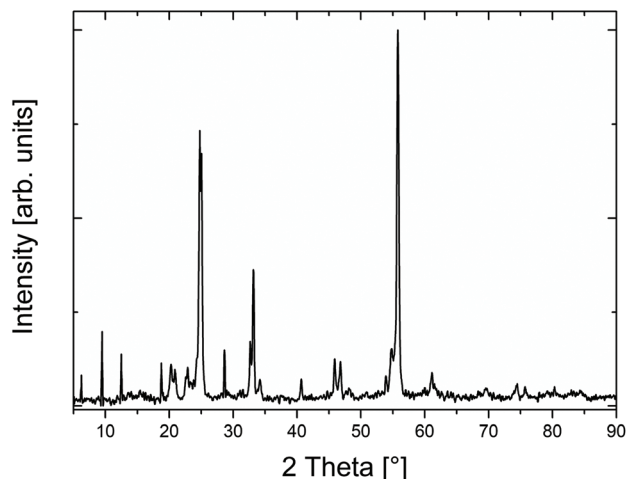
sample was neglected, because any of the low-angle peaks could not be attributed to this phase. The list of the XRD peaks with the proposed (hkl) assignations and the d values of the $W_{16}O_{47}$ structure obtained from HRTEM and from the refinement process are presented in Table 2. The calculated unit cell parameters after refinement are a = 16.04 Å, b = 3.88 Å, c = 28.48 Å and β = 96.07°. They represent the average unit cell parameters of the whole sample.

In Table 3, the unit cell parameters of $W_{16}O_{47}$ obtained from the HRTEM images, those calculated from the model,[17] and those refined from the XRD data are compared. The close

Table 2 A list of the peaks from the XRD spectrum with the proposed assignations according to the structure of $W_{16}O_{47}$. In the fifth column, the d values of the refined structure are presented, while in the last column the d values are calculated using the unit cell parameters of $W_{16}O_{47}$ obtained from the HRTEM images

| Measured 2 Theta [°]	Measured d [Å]	Measured rel. int. [arb. units]	Assigned index (hkl)	Calculated d [Å]	$W_{16}O_{47}$ d [Å]
6.20	14.24	0.07	(002)	14.16	13.94
9.48	9.32	0.20	(003)	9.44	9.29
12.48	7.09	0.11	(004)	7.08	6.97
18.76	4.73	0.10	(006)	4.72	4.65
20.28	4.38	0.10	(205)	4.40	4.47
20.88	4.25	0.08	(20$\bar{6}$)	4.26	4.26
22.88	3.88	0.08	(010)	3.88	3.80
24.80	3.59	0.70	(013)	3.59	3.52
25.00	3.56	0.63	(403)	3.54	3.74
28.64	3.11	0.14	(405)	3.11	3.24
32.68	2.74	0.14	(216)	2.75	2.73
33.16	2.70	0.33	(407)	2.70	2.78
34.20	2.62	0.05	(601)	2.62	2.80
40.68	2.22	0.05	(606)	2.22	2.33
45.92	1.97	0.10	(801)	1.97	2.11
46.80	1.94	0.10	(020)	1.94	1.90
48.12	1.89	0.03	(0 0 15)	1.89	1.86
50.88	1.79	0.02	(0 1 14)	1.79	1.76
53.92	1.70	0.04	(028)	1.70	1.67
54.84	1.67	0.12	(2 0 17)	1.67	1.58
55.80	1.65	1.00	(029)	1.65	1.62
61.12	1.52	0.06	(4 0 $\bar{1}8$)	1.52	1.50
69.56	1.35	0.02	(4 0 19)	1.35	1.35
74.48	1.27	0.03	(232)	1.27	1.25
75.72	1.13	0.03	(10 2 $\bar{1}2$)	1.13	1.15
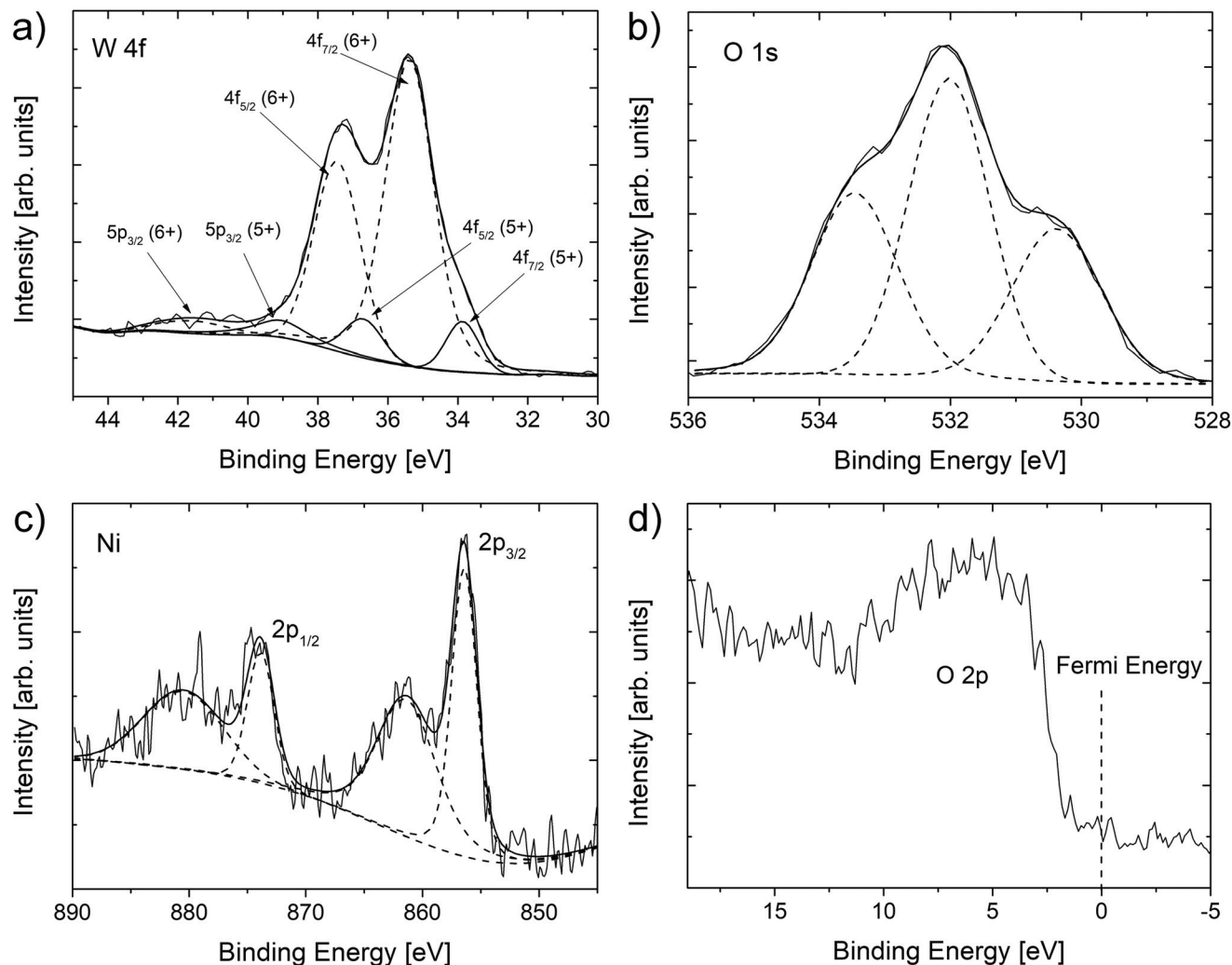
Fig. 6   XPS spectra of the platelets: (a) the W 4f core level; (b) the O 1s spectrum; (c) the Ni 2p core level; and (d) the valence band with no states at the Fermi level.

The photoelectrons from oxygen (O 1s) (Fig. 6b) form a three-peak signal. The peak at 530.4 eV corresponds to the O^{2-} oxygen bond with W^{6+} atoms. The highest intensity peak at 532.0 eV and the peak at 533.5 eV can be attributed to the bonds with tungsten in lower oxidation states. Besides W–O bonds in the CS planes, their origin could also be the C–O bonds in the adsorbed molecules, Si–O bonds in SiO_2 impurities or $Ni(OH)_2$. A weak Ni 2p signal is shown in Fig. 6c. The main peak at 856.4 eV and a satellite at 861.4 eV can be in analogy with previous studies[45,58] attributed to $Ni(OH)_2$. The valence-band spectrum (Fig. 6d) shows negligible density of states at the Fermi energy, which indicates a semiconducting behaviour of the sample.

Raman spectroscopy

The Raman spectra of WO_{3-x} materials can be divided into three frequency regions, representing different vibrational modes. Below 200 cm^{-1}, the peaks are associated with the relative translational or rotational motions of WO_6 octahedral units in the same unit cell (lattice modes), between 200 and 400 cm^{-1} the peaks are associated with the W–O–W bending modes, while in the range between 600 and 900 cm^{-1} the peaks are assigned to the W–O stretching modes.[59,60] Fig. 7 shows the optical image and Raman spectra of a platelet with the $W_{19}O_{55}$ NW situated at its edge. The spectra were taken with the laser polarisation parallel (A) and perpendicular (B) to the long axis of the $W_{19}O_{55}$ NW. The Raman shifts, relative intensities and assignations are provided in Table 4.

The Raman spectra of the $W_{19}O_{55}$ NW (Fig. 7b) show a sharp peak at 301 cm^{-1} and two overlapping broad peaks at around 695 and 740 cm^{-1}, when light polarization is parallel (A) to the b axis of the NW, and four relatively weak peaks at 107, 193, 268 and 377 cm^{-1}, and two overlapping broad peaks at 726 and 819 cm^{-1}, when polarisation is parallel to the a axis (B). The literature reports only on the peak at 319 cm^{-1}, while broad peaks at 709 cm^{-1} and 812 cm^{-1} attributed to the O–W–O stretching vibrations were recorded in annealed samples, which were oxidized at 500 °C.[41] A substantial blue shift of the
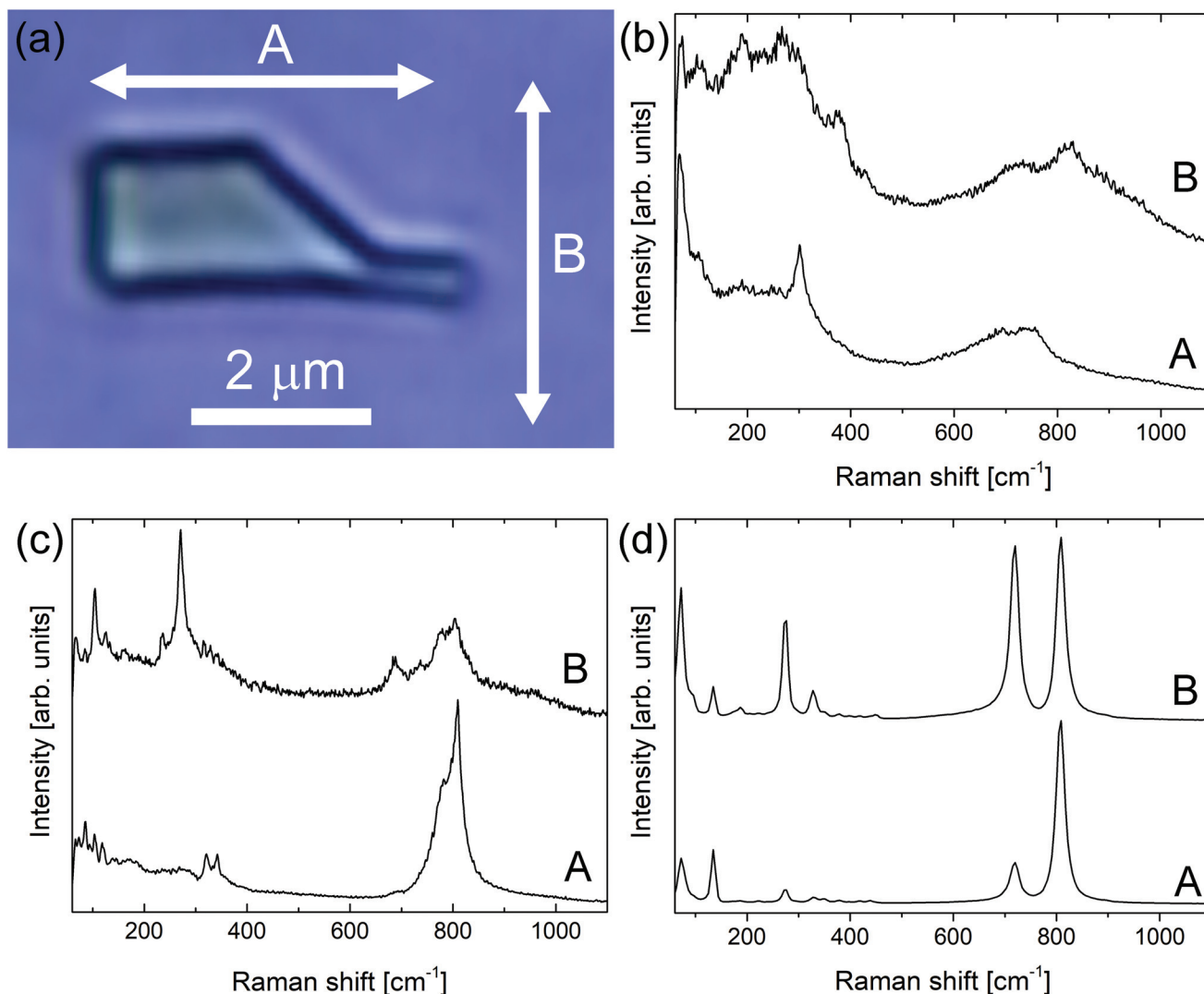
Fig. 7 (a) Optical image of a platelet with $W_{19}O_{55}$ NW at its bottom edge; (b) Raman spectra of the $W_{19}O_{55}$ NW; (c) Raman spectra of the platelets; and (d) Raman spectra of the platelets oxidized for 1 h at 873 K. The A and B arrows denote laser light polarization.

peak at 301 cm^{-1} with respect to 319 cm^{-1} is explained with even weaker chemical bonds than in the case of pure $W_{19}O_{55}$ material. Such weak chemical bonds indicate a larger degree of disorder in the structure. The broad peaks situated between 700 and 900 cm^{-1} are attributed to different W–O bond lengths in $W_{19}O_{55}$.[60,61] The almost featureless spectrum is in good agreement with the spectra from the literature.[41]

In contrast, the Raman spectra of the platelet contain more distinctive peaks (Fig. 7c). The spectrum when the polarisation of the laser is parallel to the *b* axis (A) shows three peaks at 86.5 cm^{-1}, 104.5 cm^{-1}, and 119.5 cm^{-1} assigned to the lattice modes, two peaks at 322 and 342 cm^{-1} assigned to the W–O–W bending, and a weak peak at 693 cm^{-1} and two intense peaks at 781 and 809 cm^{-1}, all associated with the W–O stretching modes. The two intense peaks are sharper and more intense pointing to a crystal structure with less defects and higher number of W–O bonds with well-defined lengths. In

the spectrum with the polarisation parallel to the *a* axis (B), the most intense peak is at 271 cm^{-1} and 12 weaker peaks in the bending and lattice mode regions are visible (Table 4). The stretching mode region has 4 peaks at similar Raman shifts to those in the spectrum (A), but less intense. The absence of Raman bands at around 950 cm^{-1} indicates that the platelets do not contain any hydrated phases and W=O groups.[46,59] The dependency of the Raman spectra on the orientation of the platelets confirms that the material has an anisotropic crystal structure.

Compared to the monoclinic m-WO$_3$,[62,63] only the Raman band of the platelet at 809 cm^{-1}, recorded with polarization along the *b* axis (A), is an exact match. This peak with the maximum intensity in the spectrum (A) was explained with the vibration of the W–O bonds with a length of 1.82 Å.[62] The second high-intensity peak in the spectrum (A) at 781 cm^{-1} is strongly red shifted with regard to 718 cm^{-1} in m-WO$_3$, which

Table 4 Raman peak position and normalized intensity of the $W_{19}O_{55}$ NWs and platelets

$W_{19}O_{55}$ A		$W_{19}O_{55}$ B		Platelets A		Platelets B		
Shift [cm^{-1}]	Rel. int. [%]	Shift [cm^{-1}]	Rel. int. [%]	Shift [cm^{-1}]	Rel. int. [%]	Shift [cm^{-1}]	Rel. int. [%]	Vibration mode
						85	7	Lattice modes
						104	27	
				86.5	21			
		107	9					
				104.5	9			
				119.5	9	125	7	
						163	6	
		193	14					
301	21					236	12	O–W–O bending modes
		268	11			271	100	
				322	11			
						316.5	7	
						328.5	6	
				342	12	340.5	6	
		377	7					
						688	16	O–W–O stretching modes
				693	3			
		726	16			737	5	
695	14							
740	14							
				781	65	777	5	
		819	25	809	100	803.5	58	

was attributed to the vibration of W–O bonds with a length of 1.88 Å.[60,62] This could represent the chemical bond length between W–O in the CS. In contrast, the Raman band at 271 cm^{-1} in the spectrum (B) is slightly blue shifted with respect to the O–W–O bending mode in m-WO$_3$ (275 cm^{-1}).

With the aim to relax the structure and compare Raman spectra, the sample was oxidized in air for 60 minutes at 873 K. The Raman spectra of the oxidized platelets are shown in Fig. 7d. The spectra in both, (A) and (B), orientations exactly match the spectra of m-WO$_3$.[62,63]

Discussion

New quasi-two-dimensional plate-like crystals were observed, which grow epitaxially on the $W_{19}O_{55}$ NWs. Six different structures were observed for the first time: $W_{18}O_{53}$ (WO$_{2.944}$), $W_{17}O_{50}$ (WO$_{2.941}$), $W_{16}O_{47}$ (WO$_{2.938}$), $W_{15}O_{44}$ (WO$_{2.933}$), $W_{14}O_{41}$ (WO$_{2.929}$) and W_9O_{26} (WO$_{2.889}$). Their unit cell parameters were determined from the HRTEM images and TEDs, and were in good agreement with the calculated ones. The $\{102\}_r$ CS planes observed in the sample are characteristic of slightly reduced WO$_{3-x}$. The stability of different WO$_{3-x}$ structures is discussed in the literature[30,31,64–68] in terms of elastic strain energy and electrostatic energy between the CS planes and the formation energy of CS planes. While some theoretical models and experimental results suggest that only a small number of W_nO_{3n-1} are stable and slightly reduced WO$_{3-x}$ will dispropor-

tionate into WO$_3$ and WO$_{2.92}$, our data show that a wide range of stoichiometries are stable at RT. As previously pointed out,[30,31,64–67] the theoretical models do not consider cation–anion and cation–cation interactions nor the polarization of the crystal which could have an important role in the stabilization of different W_nO_{3n-1} phases. It is important to note that these new phases grow together inside single platelets. This multilayer structure shows a new kind of polycrystallinity, where CS planes accommodate oxygen deficiency and relax the structure at the same time. This is evident from the appearance of a new CS plane inside the investigated platelet. Therefore, the adjacent layers could contribute to the stability of a specific phase. The surface-sensitive XPS has shown the presence of W^{5+} oxidation states typical of tungsten atoms in the CS planes. The presented W_nO_{3n-1} phases do not contain tungsten atoms in the +4 oxidation state which was experimentally shown also for W_nO_{3n-2} phases.[45] The valence-band spectrum indicates a semiconducting behaviour in agreement with recent DFT calculations.[53] Raman band shifts were observed indicating longer W–O bonds in comparison with WO$_3$ due to the creation of CS planes. The structure of these multi-stoichiometric platelets was directly resolved from the HRTEM images and modelled from electron and X-ray diffraction data. The proposed unit cell of the average structure is: a = 16.04 Å, b = 3.88 Å, c = 28.48 Å and β = 96.04°.

The literature reports[69] that Ni and WO$_3$ form a tungsten bronze, Ni$_x$WO$_3$, with a perovskite structure, similar to that of sodium tungsten bronze, Na$_x$WO$_3$. The Ni$_x$WO$_3$ structure is

stable only for $x \leq 0.035$ and crystalizes in the orthorhombic symmetry with the unit cell parameters being approximately: a = 7.4 Å, b = 7.4 Å and c = 3.8 Å. The unit cell parameter c in Ni_xWO_3 is around half of the unit cell parameter c in the monoclinic WO_3. If x is increased beyond 0.035, $NiWO_4$ is formed alongside a tungsten suboxide phase, such as $W_{18}O_{49}$ and $W_{20}O_{58}$.[69,70] If the platelets would be partially made of $NiWO_4$ or Ni_xWO_3, this would be observed in the HRTEM images and in the Raman spectra.

Conclusions

New quasi-two-dimensional tungsten oxide crystals were found to nucleate by epitaxial growth on the $W_{19}O_{55}$ nanowires as thin plate-like crystals grown up to 4 μm in lateral size. Both the nanowires and the platelets accommodate oxygen deficiency by the formation of crystallographic shear planes. Although these shear planes are equally separated in the nanowires, their distance in the platelets varies. In a single platelet, several stoichiometric phases were identified for the first time: $W_{18}O_{53}$ ($WO_{2.944}$), $W_{17}O_{50}$ ($WO_{2.941}$), $W_{16}O_{47}$ ($WO_{2.938}$), $W_{15}O_{44}$ ($WO_{2.933}$), $W_{14}O_{41}$ ($WO_{2.929}$), and W_9O_{26} ($WO_{2.889}$). The structure of these multi-stoichiometric platelets was directly resolved from the HRTEM images and modelled using electron and X-ray diffraction data. These layered crystals show a new kind of polycrystallinity, where crystallographic shear planes accommodate oxygen deficiency and at the same time contribute to the stability of a particular phase.

Experimental section

Synthesis

The platelets were synthesized by the chemical vapour transport reaction (CVT) using iodine as the transport agent and nickel as the growth promoter. The starting material consisted of 705.4 mg of WO_3 powder (Sigma-Aldrich, 99.99%), 75 mg of nickel (metal foil) and 1124 mg of iodine (1–3 mm beads, Sigma-Aldrich, 99.7). The quartz ampules were inserted into a two-zone furnace after they were evacuated (2×10^{-6} mbar) and sealed. The reaction is endothermic,[71] so the material was transported from the hot part of the ampule with a temperature of 1133 K to the colder part with a temperature of 1009 K. The transport reaction runs for 500 hours.

Raman spectroscopy

The samples were examined by Micro Raman Spectroscopy (MRS) using a WITec Alpha 300 RS scanning confocal Raman microscope in a backscattered geometry with a polarized Nd: YAG laser operating at a wavelength of 532 nm. The laser beam was focused through a $100x/0.9$ microscope objective on an area smaller than 1 μm^2. The power of the laser at the sample was approximately 1 mW. It was experimentally determined that this is the optimal power for avoiding damage or oxidation of the samples. The Raman spectra were recorded on multiple platelets with the polarization of the laser light perpendicular and parallel to the longer axis. The spectra were taken on individual platelets.

X-ray photoelectron spectroscopy

X-ray photoelectron spectroscopy (XPS) analysis was carried out using a PHI-TFA XPS spectrometer (Physical Electronics Inc.). The analysed area was 0.4 mm in diameter and about 3–5 nm in depth. The sample surface was excited by X-ray radiation from a monochromatic Al source with a photon energy of 1486.6 eV. The spectra were acquired with an energy resolution of about 1.0 eV and an analyser pass energy of 58 eV. The analysis was performed on multiple platelets deposited on carbon tape without grinding.

Transmission electron microscopy

High-resolution transmission electron microscopy (HRTEM) and electron diffraction (TED) images were acquired using a Cs probe-corrected TEM/STEM JEOL ARM 200CF microscope equipped with a cold-FEG electron source, operating at 200 kV. Distances between atomic columns and angles between their rows were measured using Digital Micrograph software. An accuracy of 0.04 Å in distance and 0.5° in angle was achieved. All HRTEM images were filtered using the Average Background Subtraction Filter method described in ref. 72.

Scanning electron microscopy

Scanning electron microscopy (SEM) images and cross-sections of the samples for TEM analysis were obtained using a Helios NanoLab 650 Focused Ion Beam-scanning electron microscope (FIB).

X-ray diffraction

X-ray diffraction (XRD) was performed at room temperature with a D4 Endeavor diffractometer (Bruker AXS) using a quartz monochromatic Cu $K_{\alpha 1}$ radiation source (λ = 0.1541 nm) and a Sol-X dispersive detector. The analysis was performed on multiple platelets dropcast on a special holder without grinding the sample.

Conflicts of interest

There are no conflicts to declare.

Acknowledgements

References

1 C. G. Granqvist, *Sol. Energy Mater. Sol. Cells*, 2000, **60**, 201–262.

2 H. Miyazaki, T. Ishigaki and T. Ota, *J. Mater. Sci. Res.*, 2017, **6**, 62.

3 Z. Hai, Z. Wei, C. Xue, H. Xu and F. Verpoort, *J. Mater. Chem. C*, 2019, **7**, 12968–12990.

4 Y. Liang, Y. Yang, C. Zou, K. Xu, X. Luo, T. Luo, J. Li, Q. Yang, P. Shi and C. Yuan, *J. Alloys Compd.*, 2019, **783**, 848–854.

5 S. S. Thind, X. Chang, J. S. Wentzell and A. Chen, *Electrochem. Commun.*, 2016, **67**, 1–5.

6 G. Kieslich, G. Cerretti, I. Veremchuk, R. P. Hermann, M. Panthöfer, J. Grin and W. Tremel, *Phys. Status Solidi*, 2016, **213**, 808–823.

7 H. Zheng, J. Z. Ou, M. S. Strano, R. B. Kaner, A. Mitchell and K. Kalantar-zadeh, *Adv. Funct. Mater.*, 2011, **21**, 2175–2196.

8 T. Vogt, P. M. Woodward and B. A. Hunter, *J. Solid State Chem.*, 1999, **144**, 209–215.

9 B. Gerand, G. Nowogrocki, J. Guenot and M. Figlarz, *J. Solid State Chem.*, 1979, **29**, 429–434.

10 L. Santos, C. M. Silveira, E. Elangovan, J. P. Neto, D. Nunes, L. Pereira, R. Martins, J. Viegas, J. J. G. Moura, S. Todorovic, *et al.*, *Sens. Actuators, B*, 2016, **223**, 186–194.

11 M. Boulova and G. Lucazeau, *J. Solid State Chem.*, 2002, **167**, 425–434.

12 V. Hariharan, B. Gnanavel, R. Sathiyapriya and V. Aroulmoji, *Int. J. Adv. Sci. Eng.*, 2019, **5**, 1163–1168.

13 A. Wolcott, T. R. Kuykendall, W. Chen, S. Chen and J. Z. Zhang, *J. Phys. Chem. B*, 2006, **110**, 25288–25296.

14 D. Chen, L. Gao, A. Yasumori, K. Kuroda and Y. Sugahara, *Small*, 2008, **4**, 1813–1822.

15 Y. Oaki and H. Imai, *Adv. Mater.*, 2006, **18**, 1807–1811.

16 N. Dirany, M. Arab, V. Madigou, C. Leroux and J. R. Gavarri, *RSC Adv.*, 2016, **6**, 69615–69626.

17 A. Magnéli, *Acta Crystallogr.*, 1953, **6**, 495–500.

18 J. G. Allpress, R. J. D. Tilley and M. J. Sienko, *J. Solid State Chem.*, 1971, **3**, 440–451.

19 S. Iijima, *J. Solid State Chem.*, 1975, **14**, 52–65.

20 L. A. Bursill and B. G. Hyde, *J. Solid State Chem.*, 1972, **4**, 430–446.

21 T. Miyano, M. Iwanishi, C. Kaito and M. Shiojiri, *Jpn. J. Appl. Phys.*, 1983, **22**, 863.

22 M. M. Dobson and R. J. D. Tilley, *Acta Crystallogr., Sect. B: Struct. Sci.*, 1988, **44**, 474–480.

23 W. Merchan-Merchan, M. F. Farahani and Z. Moorhead-Rosenberg, *Micron*, 2014, **57**, 23–30.

24 J. Booth, T. Ekström, E. Iguchi and R. J. D. Tilley, *J. Solid State Chem.*, 1982, **41**, 293–307.

25 M. Sundberg and R. J. D. Tilley, *J. Solid State Chem.*, 1974, **11**, 150–160.

26 R. J. D. Tilley, *Mater. Res. Bull.*, 1970, **5**, 813–823.

27 M. Sundberg, *Acta Crystallogr., Sect. B: Struct. Crystallogr. Cryst. Chem.*, 1976, **32**, 2144–2149.

28 Y. A. Barabanenkov, N. D. Zakharov, I. P. Zibrov, V. P. Filonenko, P. Werner, A. I. Popov and M. D. Valkovskii, *Acta Crystallogr., Sect. B: Struct. Sci.*, 1993, **49**, 169–171.

29 R. J. D. Tilley, *J. Solid State Chem.*, 1976, **19**, 53–62.

30 E. Iguchi and R. J. D. Tilley, *Philos. Trans. R. Soc., A*, 1977, **286**, 55–85.

31 E. Iguchi and R. J. D. Tilley, *J. Solid State Chem.*, 1980, **32**, 221–231.

32 R. Pickering and R. J. D. Tilley, *J. Solid State Chem.*, 1976, **16**, 247–255.

33 L. Zhang, H. Wang, J. Liu, Q. Zhang and H. Yan, *J. Mater. Sci.: Mater. Electron.*, 2019, 1–13.

34 E. Gebert and R. J. Ackermann, *Inorg. Chem.*, 1966, **5**, 136–142.

35 P. Labbe, in *Key Engineering Materials*, 1992, vol. 68, p. 293.

36 J. M. Berak and M. J. Sienko, *J. Solid State Chem.*, 1970, **2**, 109–133.

37 S. K. Deb, *Phys. Rev. B: Solid State*, 1977, **16**, 1020.

38 T. Soltani, A. Tayyebi, H. Hong, M. H. Mirfasih and B.-K. Lee, *Sol. Energy Mater. Sol. Cells*, 2019, **191**, 39–49.

39 F. Peng, S. Wang, W. Yu, T. Huang, Y. Sun, C. Cheng, X. Chen, J. Hao and N. Dai, *J. Mater. Sci.: Mater. Electron.*, 2020, 1–9.

40 Z. Shen, Z. Zhao, J. Wen, J. Qian, Z. Peng and X. Fu, *J. Nanomater.*.

41 J. Qian, Z. Zhao, Z. Shen, G. Zhang, Z. Peng and X. Fu, *RSC Adv.*, 2016, **6**, 8061–8069.

42 M. Ling, C. S. Blackman, R. G. Palgrave, C. Sotelo-Vazquez, A. Kafizas and I. P. Parkin, *Adv. Mater. Interfaces*, 2017, **4**, 1700064.

43 S. Heo, C. J. Dahlman, C. M. Staller, T. Jiang, A. Dolocan, B. A. Korgel and D. J. Milliron, *Nano Lett.*.

44 A. Polaczek, M. Pekala and Z. Obuszko, *J. Phys.: Condens. Matter*, 1994, **6**, 7909.

45 M. Remškar, J. Kovac, M. Viršek, M. Mrak, A. Jesih and A. Seabaugh, *Adv. Funct. Mater.*, 2007, **17**, 1974–1978.

46 G. L. Frey, A. Rothschild, J. Sloan, R. Rosentsveig, R. Popovitz-Biro and R. Tenne, *J. Solid State Chem.*, 2001, **162**, 300–314.

47 B.-O. Marinder, *Angew. Chem., Int. Ed.*, 1986, **25**, 431–442.

48 Arne Magneli, *Acta Chem. Scand.*, 1948, **2**, 501–517.

49 M. Sato, M. Onoda and Y. Matsuda, *J. Phys. C: Solid State Phys.*, 1987, **20**, 4763.

50 Z. Fang, S. Jiao, B. Wang, W. Yin, S. Liu, R. Gao, Z. Liu, G. Pang and S. Feng, *Mater. Today Energy*, 2017, **6**, 146–153.

51 G. Wang, Y. Ling and Y. Li, *Nanoscale*, 2012, **4**, 6682–6691.

52 C. Rosique-Pérez, J. González-Calbet, M. Vallet-Regí and M. A. Alario-Franco, *J. Solid State Chem.*, 1988, **76**, 313–318.

53 Y.-J. Lee, T. Lee and A. Soon, *Chem. Mater.*, 2019, **31**, 4282–4290.

54 H. A. Wriedt, *Bull. Alloy Phase Diagrams*, 1989, **10**, 368–384.

55 C. J. Marvel, D. Yin, P. R. Cantwell and M. P. Harmer, *Mater. Sci. Eng., A*, 2016, **664**, 49–57.

56 D. Briggs, *Surf. Interface Anal.*, 1981, **3**, 146–147.

57 M. Katoh and Y. Takeda, *Jpn. J. Appl. Phys.*, 2004, **43**, 7292.

58 A. N. Mansour, *Surf. Sci. Spectra*, 1994, **3**, 239–246.

59 M. F. Daniel, B. Desbat, J. C. Lassegues, B. Gerand and M. Figlarz, *J. Solid State Chem.*, 1987, **67**, 235–247.

60 F. D. Hardcastle and I. E. Wachs, *J. Raman Spectrosc.*, 1995, **26**, 397–405.

61 J. M. Gonzalez-Calbet, C. Rosique-Perez, M. Vallet-Regi, M. A. Alario-Franco and J. Rodríguez-Carvajal, *Solid State Ionics*, 1989, **32**, 162–166.

62 K. Thummavichai, N. Wang, F. Xu, G. Rance, Y. Xia and Y. Zhu, *R. Soc. Open Sci.*, 2018, **5**, 171932.

63 E. Salje, *Acta Crystallogr., Sect. A: Cryst. Phys., Diffr., Theor. Gen. Crystallogr.*, 1975, **31**, 360–363.

64 E. Iguchi and R. J. D. Tilley, *J. Solid State Chem.*, 1977, **21**, 49–56.

65 E. Iguchi, E. Salje and R. J. D. Tilley, *J. Solid State Chem.*, 1981, **38**, 342–359.

66 E. Iguchi and R. J. D. Tilley, *J. Solid State Chem.*, 1978, **24**, 121–130.

67 E. Iguchi and R. J. D. Tilley, *J. Solid State Chem.*, 1978, **24**, 131–141.

68 E. Iguchi, H. Sugimoto, A. Tamenori and H. Miyagi, *J. Solid State Chem.*, 1991, **91**, 286–295.

69 M. Pouchard, J. P. Chaminade, J. P. Doumerc, J. C. Launay and P. Hagenmuller, *Mater. Res. Bull.*, 1972, 7, 223–231.

70 K. T. Jacob, *J. Mater. Sci.*, 1977, **12**, 1647–1652.

71 P. Schmidt, M. Binnewies, R. Glaum and M. Schmidt, in *Advanced Topics on Crystal Growth*, IntechOpen, 2013.

72 R. Kilaas, *J. Microsc.*, 1998, **190**, 45–51.